Check for updates

Metal free and efficient photoelectrocatalytic removal of organic contaminants over g-C$_3$N$_4$ nanosheet films decorated with carbon quantum dots

Zisheng Zhang,[ac] Shuanglong Lin,[a] Xingang Li,[ad] Hong Li[*a] and Wenquan Cui [iD] [*b]

As a typical metal-free semiconductor photocatalyst, a composite photocatalyst comprised of g-C$_3$N$_4$ nanosheets decorated with carbon quantum dots (CQDs/g-C$_3$N$_4$) was synthesized via a simple ultrasonic dispersion self-assembly method. The structure of the photocatalyst was determined by powder X-ray diffraction and transmission electron microscopy. The photoelectrocatalytic properties of the photocatalyst were examined under visible light irradiation for the degradation of methylene blue (MB) and phenol. The results indicate that the photoelectrocatalytic activities of the CQD/g-C$_3$N$_4$ composites are dependent on the CQD loading quantity. The highest photoelectrocatalytic performance observed from the CQD/g-C$_3$N$_4$ composites was a MB degradation of 97.21% after 3 h of irradiation. A photoelectrocatalytic mechanism for the degradation of MB over the CQDs/g-C$_3$N$_4$ was proposed based on the above. Our results provide an invaluable methodology for the design of a highly visible light-responsive photocatalyst based on CQD/non-metallic material and related functional materials. The metal-free photocatalyst is low-cost, shows thermal and chemical stability, and comprises earth-abundant and environmentally friendly materials, and is promising for semiconductor composites and new energy applications.

1. Introduction

Substantial research interest has been attracted by ultrathin two-dimensional (2D) materials in recent years due to their fascinating properties as well as their enormous applicability to areas such as energy storage devices, photovoltaics, catalysis, and electronics.[1–4] Among corresponding bulk materials, two-dimensional materials with thicknesses approaching the atomic level display the characteristics of an atomic structure, such as the degree of atomic disorder, bond length and coordination number, which would subsequently affect the physicochemical properties of a material.[5]

Recently, C$_3$N$_4$ has drawn attention as a promising new layered material, due to the low toxicity, excellent stability and high photocatalytic performance. As the most stable allotrope of carbon nitride, graphitic carbon nitride (g-C$_3$N$_4$) has a narrow E_g

of 2.7 eV due to the sp^2 hybridization of carbon and nitrogen, forming π-conjugated graphitic planes.[6] Wang et al. first researched the application of g-C$_3$N$_4$ in photocatalytic wastewater splitting under visible light irradiation in 2009.[7] This semiconductor photocatalyst is metal-free, and has relatively high chemical and thermal stabilities, with an appropriate conjugate structure that has been used as a reliable scaffold for photocatalysis.[8,9] Nevertheless, the high recombination rate of the photoinduced e$^-$–h$^+$ pairs and small specific surface area of g-C$_3$N$_4$ result in a low photocatalytic performance.[10,11]

Over the years, non-metallic carbon materials with high conductivities such as graphene,[12–14] graphene oxide,[15,16] mesoporous carbon and carbon nanotubes[17,18] have been coupled with g-C$_3$N$_4$ to act as electron acceptors to separate the e$^-$–h$^+$ pairs.[19] However, it is still a hot research topic to improve the efficiency of g-C$_3$N$_4$-based visible light photocatalysts for industrial applications. Therefore, the design of more efficient and stable photocatalysts that can meet the requirements for practical environmental purification represents the central challenge of research in photocatalysis.

As a newly discovered novel carbon nanomaterial, carbon quantum dots (CQDs) possess abundant photo-physical performances. They have been applied in many research fields from catalysis to electronics and others due to their low cost, excellent stability, and superior biocompatibility, as well as

[a]School of Chemical Engineering and Technology, Tianjin University, Tianjin, PR China, 300072. E-mail: lihongtju@tju.edu.cn; Tel: +86-315-2592169; +86-22-27404701

[b]College of Chemical Engineering, North China University of Science and Technology, Tangshan, PR China, 063009. E-mail: wkcui@163.com

[c]Department of Chemical & Biological Engineering, University of Ottawa, 161 Louis Pasteur St., Ottawa, Canada K1N6N5

[d]National Engineering Research Center of Distillation Technology, Tianjin, PR China, 300072

their electron-transport and -accepting properties.[20] CQDs have most recently been applied to photocatalytic systems.[21,22] Their size effect and fluorescence properties further improve their photocatalytic performance.[23,24] Numerous studies have indicated that the electron-transport and -accepting properties of CQDs may be advantageous to guide the flow of photogenerated charges; therefore, significant photocatalytic properties may be obtained by means of the construction of semiconductor/ carbon composites.[25,26]

CQDs have been combined with hematite, BiOX (X = Br or Cl),[27,28] Bi_2WO_6,[29] $BiVO_4$,[30] C_3N_4,[31] Ag_3PO_4,[32] and TiO_2(ref. 33) for the photocatalytic oxidation (PCO) of organic pollutants in aqueous solutions. Considering the small size of CQDs and the ultrathin structure of g-C_3N_4 nanosheets, the contact area between g-C_3N_4 nanosheets and CQDs may be greatly increased. Therefore, nanoscale junctions under close contact may be established. Photogenerated charges may transmit rapidly to the surface and further travel to the CQDs. Therefore, an efficient charge separation may be achieved with CQD/g-C_3N_4 ultrathin nanosheet composites. As a metal-free composite photocatalyst, CQD/g-C_3N_4 comprises earth-abundant and environmentally friendly materials, is low-cost, and shows thermal and chemical stability.

However, there have been no reports on the photoelectrocatalytic (PEC) degradation of organic pollutants on CQD/g-C_3N_4 composites under visible light irradiation, and the corresponding mechanism still remains confusing. Therefore, in this study we report the fabrication of visible light-driven g-C_3N_4 ultrathin nanosheets decorated with CQDs on indium-tin oxide (ITO) glass by a simple dipping process at room temperature. Photocatalysis was considered and combined with electrochemical oxidation, which improved the activity of the CQDs/ g-C_3N_4 to enhance the mineralization of organic pollutants through a synergistic photoelectric effect. In a photoelectrocatalytic (PEC) system, a potential bias which acts on the photoanode could provide an external pushing force that could accelerate photogenerated e$^-$ to move faster to the cathode through the external circuit. Thus, the separation efficiency for photogenerated e$^-$–h$^+$ pairs is promoted.[34,35] What's more, due to the advantages of the combination of heterogeneous photocatalysis (PC) with electrocatalytic (EC) processes, the PEC process is more efficient for organic pollutant degradation compared to pure EC and PC processes.

2. Experimental

2.1. Photocatalyst synthesis

Synthesis of the g-C_3N_4 nanosheets. Synthesis of g-C_3N_4 powder was accomplished *via* a reported process.[36] 10 g of melamine powder was heated to 550 °C in a covered alumina crucible at a rate of 2 °C min^{-1} in a tube furnace, and held at 550 °C for 4 h. All of the experiments were performed in air. The yellow bulk mass was ground into a powder for use in the next step. Ultrathin g-C_3N_4 nanosheets were prepared by liquid exfoliation of bulk g-C_3N_4 in water. Specifically, 50 mg of bulk g-C_3N_4 powder was dispersed in 50 mL of distilled water and then ultrasonicated for approximately 24 h. The suspension liquid

was then centrifuged at 2000 rpm to remove the large particles of unexfoliated g-C_3N_4. The resulting suspension liquid of ultrathin g-C_3N_4 nanosheets was collected for use in the next step.

Synthesis of the carbon quantum dots (CQDs).[37] Two parallel graphite rods with a separation of 7.5 cm were inserted into deionized water as the anode and counter-electrode (18.4 MΩ cm^{-1}, 400 mL). A direct current (DC) power supply provided a 30 V static potential to the two electrodes. The anode graphite rod became corroded, and the solution gradually became dark yellow with continuous stirring. The electrolyte was filtered with slow-speed quantitative filter paper, and then the filtrate was centrifuged at 22 000 rpm for 30 min, which could remove the graphite particles and graphite oxide. The resultant solution consisted of water soluble CQDs.

Preparation of the CQD/g-C_3N_4 photocatalysts. CQD/g-C_3N_4 composites were synthesized by a simple method. 100 mg of g-C_3N_4 nanosheets was added to 50 mL of deionized water under ultrasonic treatment for 1 h. Next, a defined volume of CQD solution (1, 3, 5, 7 and 9 mL) was added to the above solution, and then stirred for 90 min at room temperature to create a clear dispersion of the CQDs. The obtained samples were labeled as 1-CQD/g-C_3N_4, 3-CQD/g-C_3N_4, 5-CQD/g-C_3N_4, 7-CQD/ g-C_3N_4 and 9-CQD/g-C_3N_4, respectively. The CQD/g-C_3N_4 photocatalysts were removed by filtration, washed with ethanol several times and dried for further characterization.

Synthesis of the CQD/g-C_3N_4 film electrode. A dip-coating method was used to prepare the CQD/g-C_3N_4 films on indium-tin oxide (ITO) glass.[38] Firstly, 100 mg of the CQD/g-C_3N_4 film powder was dissolved in 100 mL of polyethylene glycol, ethyl alcohol, and water, and then ultrasonicated for 6 h. The glass-substrate was placed in the CQD/g-C_3N_4 dispersion and then pulled through according to the parameters: a lift height of 35 mm, a dipping–pulling rate of 50 μm s^{-1}, a residence time of 30 s and an immersion time of 60 s, with the steps repeated three times. The product was dried for 30 min at 80 °C after each pull through.

2.2. Photocatalyst characterization

X-ray diffractometry (XRD) was used to determine the crystal structures and phase data of the samples. Scanning electron microscopy (SEM) (Hitachi, s-4800), energy dispersive X-ray spectroscopy (EDX), and transmission electron microscopy (TEM) (JEOL Ltd., JEM-2010) were used to investigate the morphologies of the samples. The photoluminescence of the powder samples was measured using a spectrofluorometer (Hitachi, f7000). A Perkin Elmer System 2000 infrared spectrometer provided the Fourier transform infrared (FTIR) spectra with KBr as the reference sample. A three-electrode quartz cell system was used to perform the electrochemical and photoelectrochemical measurements. A CHI 660B electrochemical system was used to record the photoelectrochemical results.

2.3. Photoelectrocatalytic activity

To evaluate the efficiency of the photoelectrocatalytic (PEC) degradation and the stability of the CQD/g-C_3N_4 film electrodes,

methylene blue (MB: 5 mg L^{-1}, 100 mL) and phenol (5 mg L^{-1}, 100 mL) were used as model pollutants. In the PEC degradation experiments, a CHI 660E Electrochemical Workstation (Shanghai Chenhua Instrument Corp., China) was used to carry out all of the photoelectrochemical experiments *via* a conventional three-electrode quartz cell system at room temperature. A 500 W Xe lamp (Beijing Changtuo Co. Ltd.) purchased with a UV cut-off filter (420 nm) was used for the light source. The as-prepared photoelectrode was used as a working electrode, while Pt was used as a counter electrode and a saturated calomel electrode (SCE) was used as the reference electrode. Typical PEC degradation was conducted under visible light irradiation in 0.1 M Na$_2$SO$_4$ containing one of the two model pollutants. After incubating in the absence of irradiation for 30 min to establish an absorption/desorption equilibrium, the reactions were initiated under illumination with visible light. The concentrations of the collected MB solutions were analyzed using a UV-vis spectrophotometer. Meanwhile, the concentration of phenol was determined using high-performance liquid chromatography (HPLC).

3.   Results and discussion

3.1.   Characterization of the catalysts

XRD analysis was carried out to investigate the crystal structures and phases of the as-prepared films, the results of which are displayed in Fig. 1. Fig. 1 displays the XRD diffraction peaks of pure g-C$_3$N$_4$ alongside those of the CQD/g-C$_3$N$_4$ samples with different CQD content. All of the samples possess two characteristic peaks at 13.2° and 27.7°, which may be indexed as graphitic carbon nitride for the (100) and (002) crystal facets, respectively (JCPDS card no: 87-1526). The obvious characteristic peak at 27.7° (002) corresponding to a lattice spacing of 0.32 nm reflects the inter-planar accumulation of aromatic rings, meanwhile the peak located at 13.2° (100) is from the in-plane repeated tri-*s*-triazine units.[39] Additionally, a weaker peak of the (006) crystal facets (JCPDS card no: 48-1206) at 31.1° may correspond to carbon, and the peak intensity slightly increases with an increase in the loading amount of the CQDs. It should be obvious that no other characteristic peaks of the CQDs were discovered in the CQD/g-C$_3$N$_4$ samples, due to the low quantities.
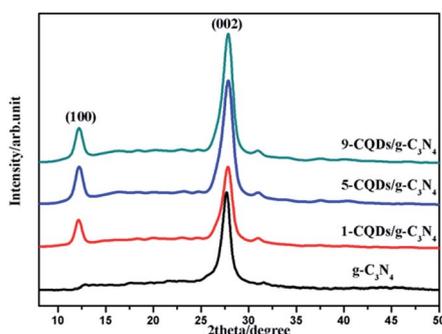
Fig. 2 shows clear SEM and TEM images of the CQD/g-C$_3$N$_4$ films. As shown in Fig. 2a and b, the cross-sectional morphology of the SEM images was analysed. It can be seen that the CQD/g-C$_3$N$_4$ film thickness on the ITO base was determined to be about 1.5 μm. The picture of the CQD/g-C$_3$N$_4$ film electrode is shown in the inset of Fig. 2a. The CQD/g-C$_3$N$_4$ composite uniformly covers the entire surface of the ITO substrate with a layered accumulation, meanwhile there are uncovered, small areas and overlapping patches. However, the CQDs/g-C$_3$N$_4$ were observed to be compactly adhered on the ITO substrate through calcination at 300 °C for 30 min, and the morphology of the samples was not damaged. Additionally, in the EDX spectrum of the CQDs/g-C$_3$N$_4$ (Fig. 2c), C and N are both observed, with the
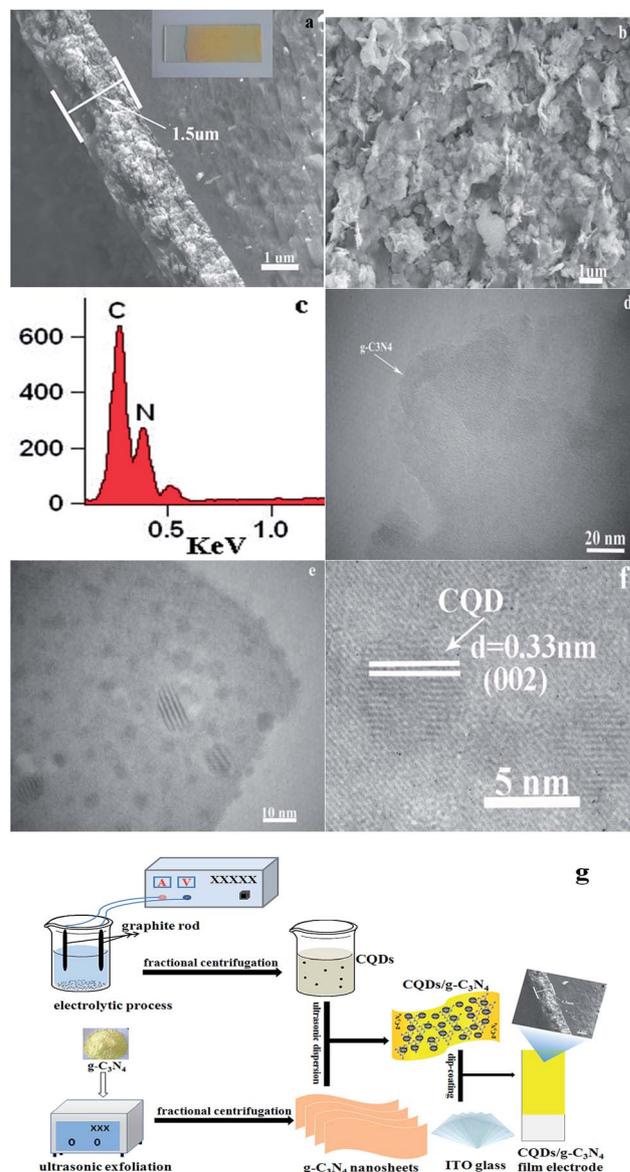

Fig. 2 Cross-section (a) and surface images (b) of the CQD/g-C$_3$N$_4$ film electrode; (c) EDX spectrum of the CQDs/g-C$_3$N$_4$; (d) TEM image of the g-C$_3$N$_4$ nanosheets; (e and f) TEM images of the CQDs/g-C$_3$N$_4$; and (g) schematic illustration for the preparation of the CQD/g-C$_3$N$_4$ film electrode.

Fig. 1 XRD patterns of the different films.

content of C exceeding that of N. Fig. 2d presents a TEM image of the g-C_3N_4 nanosheets, the nanosheet structures of which are nearly transparent. A large number of CQDs (2–10 nm) are seen to be uniformly distributed across the surface of g-C_3N_4 in Fig. 2e and f. The HRTEM image (Fig. 2f) of a CQD crystallite shows a 0.33 nm lattice spacing, which corresponds to the (002) crystallographic plane of graphitic carbon.[40] The above results suggest that the g-C_3N_4 nanosheets have been successfully decorated by CQDs to form the CQDs/g-C_3N_4. Fig. 2g depicts the schematic illustration for the preparation of the CQD/g-C_3N_4 film electrode, which gives a direct and clear picture of the synthetic process.

The SEM image and corresponding EDX mapping images (Fig. 3) further show the uniform dispersion of C, N and O, in which the mappings are similar to the SEM morphology image (Fig. 3a) of the CQDs/g-C_3N_4. The elemental mapping of the CQDs/g-C_3N_4 displays the uniform distribution of the elements of C and O on the surface of g-C_3N_4. The elements of C and O are from the CQDs. The results further indicate that the CQDs have been successfully modified on the surface of g-C_3N_4.

The optical reflectance spectra of g-C_3N_4 and the CQD/g-C_3N_4 composites were recorded using a UV-vis spectrometer. As Fig. 4a shows, the absorption point for g-C_3N_4 occurs at approximately 450 nm. After combining with the CQDs, an obvious red-shift of the absorption edge occurred in comparison to that of g-C_3N_4. The obtained CQD/g-C_3N_4 samples exhibited a wide visible light absorption region and an enhanced light absorption intensity. These results indicate that the CQD-modified g-C_3N_4 samples may be excited to generate more e^-–h^+ pairs under identical irradiation conditions, and may therefore result in a higher photocatalytic activity.[41] The E_g was estimated on account of the absorption curve for crystalline semiconductors obeying the following formula:
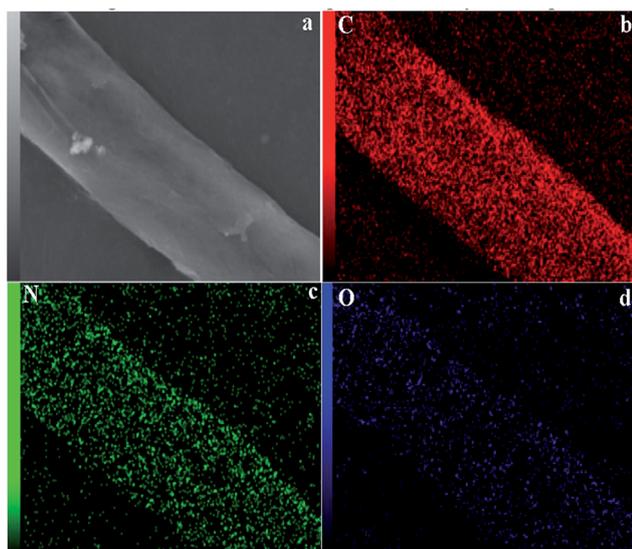
$$\alpha h\nu = A(h\nu - E_g)^n$$

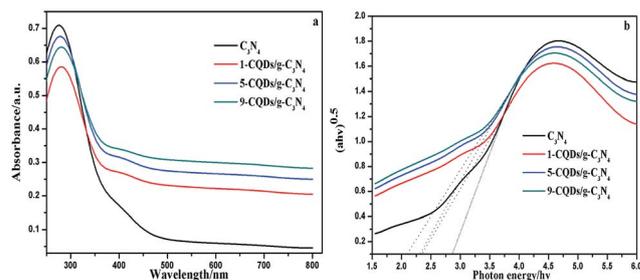Fig. 3 (a) SEM image and (b–d) EDX mapping images of CQDs/g-C_3N_4.

Fig. 4 (a) UV-vis diffuse reflectance spectra of g-C_3N_4 and the CQD/g-C_3N_4 composites with different quantities of the CQDs. (b) The relationship of $(\alpha h\nu)^{1/2}$ versus photon energy.

where A, ν, α, E_g and h are a constant, the frequency, the absorption coefficient, the band gap energy, and Planck's constant, respectively. As is well known, n depends on whether the optical transition of the semiconductor is indirect ($n = 2$) or direct ($n = 1/2$).[42] Due to the optical transition for g-C_3N_4 being indirect,[43] the value of n is 2. From the curves in Fig. 4b, the E_g of g-C_3N_4 can be seen to decrease from 2.8 to 2.1 eV after being decorated with the CQDs. This implies that sub-band energy levels may exist between the CQDs and g-C_3N_4 in the bandgaps of the CQD/g-C_3N_4 composites.[44] This assumption is further proven by the PL spectra (Fig. 5).

The migration and capture rates of the photoinduced carriers could be determined via the photoluminescence (PL) spectrum which is formed by e^-–h^+ recombination.[45] As can be seen in Fig. 5 in the range of 300–510 nm, both g-C_3N_4 and the CQDs/g-C_3N_4 exhibit an evident emission peak at approximately 360 nm with a 275 nm excitation wavelength. Here, the photoluminescence intensities decreased in the order of g-C_3N_4 > CQDs/g-C_3N_4. The emission peak at 360 nm for g-C_3N_4 may be due to the recombination of the CB electrons with the VB holes. The peak remained at the same wavelength upon the combination of g-C_3N_4 with the CQDs; however, the intensity decreased, suggesting that the introduction of the CQDs inhibited the charge recombination.

The PL spectra of the CQDs were generated by excitation wavelength light. As is shown in Fig. 6a, it is clear that the carbon quantum dots exhibited particularly remarkable emission peaks when the excitation wavelength was changed from 300 to 340 nm. When the excitation wavelength is tuned from
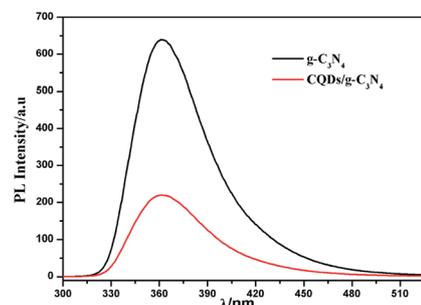

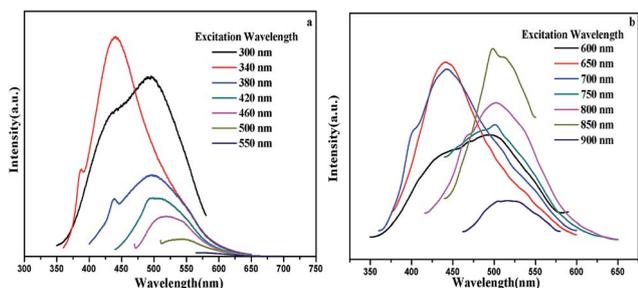Fig. 5 PL spectra of g-C_3N_4 and the CQDs/g-C_3N_4.

Fig. 6 PL curve of the CQDs excited by different wavelengths of light.

380 to 550 nm, the fluorescence spectrum peaks undergo an obvious red-shift with a gradual intensity decrease. The above results show that the CQDs have strong fluorescence up-conversion properties. In addition to the strongly decreasing intensity associated with the PL behavior, Fig. 6b shows the fluorescence spectrum peaks of the CQDs excited by long wavelengths. The down-conversion PL spectra show an excitation-dependent PL feature similar to the up-conversion spectra. When the excitation wavelengths are increased from 600 to 900 nm, the down-converted emission peaks exhibit a red shift from 430 to 520 nm. Combining the above results and reports of CQDs, the up-conversion and down-conversion properties of the CQDs may be due to a two-photon absorption process.[46,47]

FTIR spectroscopy and XPS were used to further investigate the chemical bonding of the samples. Fig. 7 shows the FTIR spectra of the as-prepared samples. It can be observed that the pure CQDs exhibited characteristic peaks at 2940, 2870 and 1720 cm^{-1}, corresponding to sp^2 and sp^3 C–H and –COOH vibrations, respectively.[48,49] The spectra of pure g-C$_3$N$_4$ and the CQDs/g-C$_3$N$_4$ are similar, showing that the chemical structure of g-C$_3$N$_4$ does not change with the decoration of the CQDs. Specifically, the characteristic peak between 3600 and 3000 cm^{-1} may be due to N–H stretching, as there are a few hydrogenated N atoms present in the g-C$_3$N$_4$ nanosheets. The characteristic peaks at 1643, 1569, 1469, 1409, 1317 and 1239 cm^{-1} correspond to C=N and C–N stretching vibration modes. Both the g-C$_3$N$_4$ and CQD/g-C$_3$N$_4$ spectra show a sharp breathing peak at 807 cm^{-1} which is attributed to the triazine units.
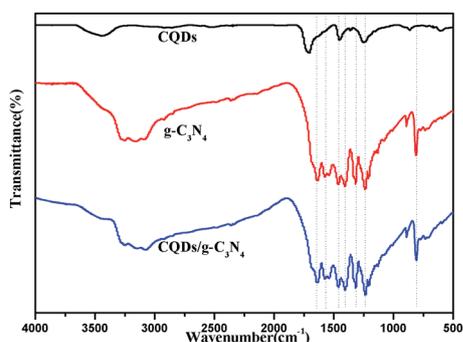
The surface chemical composition of the CQDs/g-C$_3$N$_4$ was analysed using X-ray photoelectron spectroscopy (XPS). Fig. 8a shows the XPS survey scan of the CQDs/g-C$_3$N$_4$, indicating the presence of C, N and O with no other impurities. The C 1s XPS spectrum of the CQDs/g-C$_3$N$_4$ was deconvoluted into two different components (Fig. 8b), with the two peaks located at 288.0 and 284.5 eV being assigned to the sp^2 carbon (N–C=N) and graphitic carbon (C–C) modes, respectively.[50,51] The N 1s spectrum is shown in Fig. 8c, and displays four diffraction peaks located at 405.4, 400.1, 398.9 and 398.0 eV. The obvious N 1s signal peak at 398.0 eV may be attributed to sp^2 hybridized aromatic N found in the triazine units. The quaternary N bound to three carbon atoms in the aromatic structure may correspond to the weak peak located at 400.1 eV.[52,53] The diffraction peak of the tertiary N in N(C)$_3$ or H–N–(C)$_2$ is at 398.9 eV. Lastly, the O 1s peak (Fig. 8d) located at 531.4 eV can be deconvoluted into three peaks. The peaks located at 532.4 and 531.1 eV can be attributed to adsorbed water and –OH, respectively. The peak located at 530.2 eV corresponds to lattice oxygen.

The superiority of the photoelectrocatalytic degradation could be proven through a series of degradation experiments in a three-electrode configuration photoelectrochemical cell (PEC) with a 500 W xenon lamp. The supporting electrolyte contained 5 ppm MB and 0.1 M Na$_2$SO$_4$. The EC experiment was performed with a bias potential of 1.0 V in the absence of illumination. The photoelectrocatalytic measurements were conducted under a bias potential of 1.0 V with illumination. From Fig. 9a, it can be seen that the concentration of MB remains relatively constant in the blank reaction, indicating that MB is a stable target object. Additionally, it can be seen that MB is barely degraded under the bias potential in the absence of illumination. On the contrary, degradation is quite evident in the presence of irradiation, and an enhanced degradation efficiency is observed under photoelectrodegradation. Compared to other degradation processes, the CQD/g-C$_3$N$_4$
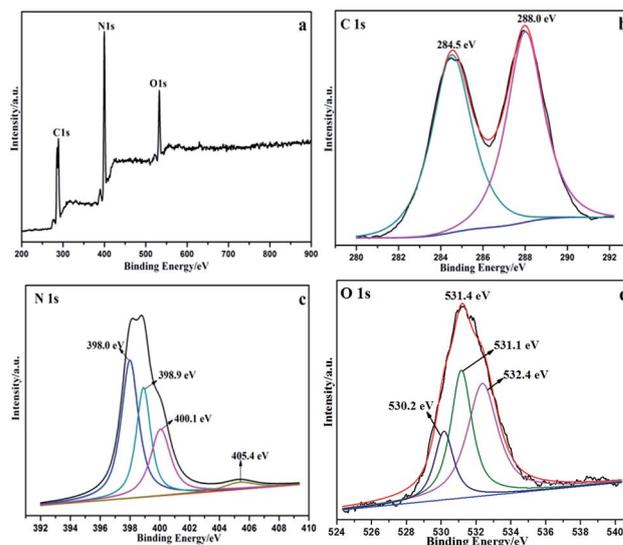

Fig. 8 XPS spectra of the CQD/g-C$_3$N$_4$ materials. (a) Survey of the sample; (b) C 1s; (c) N 1s; and (d) O 1s.

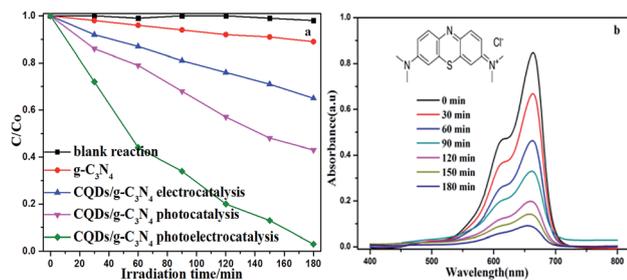**Fig. 7** FTIR spectra of the CQDs, g-C$_3$N$_4$ and the CQDs/g-C$_3$N$_4$.

Fig. 9 (a) Different MB degradation processes over the g-C$_3$N$_4$ and CQD/g-C$_3$N$_4$ photoelectrodes (MB: 5 ppm, 100 mL; Na$_2$SO$_4$: 0.1 M); (b) absorption spectra for the MB solution in the presence of the CQD/g-C$_3$N$_4$ photoelectrode under visible light irradiation.

photoelectrodes showed the highest degradation efficiency (97.2%), whereas the electrocatalytic (EC) and photocatalytic (PC) degradation efficiencies of the CQDs/g-C$_3$N$_4$ were only 35.4% and 57.02%, respectively, for the same time period. Additionally, the photoelectrocatalytic activity of g-C$_3$N$_4$ is relatively low (11.1%), due to the high recombination of the photogenerated e$^-$–h$^+$ pairs. This suggests that the synergy of the bias potential and illumination is beneficial for the separation of the electron–hole pairs, and thus enhances the degradation performance. Fig. 9b shows temporal changes to the absorption curve for the MB solutions under visible light in the presence of the CQDs/g-C$_3$N$_4$. This shows that the intensity of the characteristic intensity curve located at 664 nm reduces with the irradiation time being increased. Additionally, after about 180 minutes of irradiation, the color of the MB solutions gradually faded from dark blue to pale blue or even colourless, which implies the extent of destruction of the MB molecular structure.

Fig. 10a shows the photoelectrocatalytic degradation of MB on different electrodes. As for the CQD/g-C$_3$N$_4$ composites, the MB degradation efficiency was found to increase as the CQD content was increased. When the CQD content was increased to 5 mL (5-CQDs/g-C$_3$N$_4$), the MB degradation efficiency reached a maximum of 97.2% (0.0177 min^{-1}, Fig. 10b). With the CQD content increasing, the photoelectrocatalytic degradation activity of the composite was observed to decrease, with 9-CQDs/g-C$_3$N$_4$ having a degradation efficiency of 87% (0.0104 min^{-1}, as shown in Fig. 10b) under visible light

irradiation. It is possible that when the CQD content is sufficiently high, there is an associated decrease in the number of available active sites, and thus a lower photoelectrocatalytic activity.[54] In such a situation, excess CQDs could act as recombination sites for electron–hole pairs. Therefore, the optimal quantity of the CQDs was found to be 5 mL. At this point, agglomeration of the CQDs is negligible, and the surface reaction active sites are reduced.

As is known, the photoelectrocatalytic degradation process for low concentrations of organic pollutants follows pseudo first-order kinetics.[55] The 5-CQD/g-C$_3$N$_4$ composite was used to study the PEC degradation of MB. Different potentials (0.0, 0.5, 1.0, 1.5 and 2.0 V) were used to observe the MB PEC degradation process under visible light irradiation. The degradation rate constants of the different bias voltages for the MB degradation are shown in Fig. 11. The degradation efficiency was found to gradually increase as the bias potential was increased from 0.0 to 1.0 V. The PEC degradation rate is up to 97.2% (0.018 min^{-1}) with a 1.0 V bias voltage. However, the degradation rate decreased when the bias voltage was further increased, dropping to 88.4% at 2.0 V, which may be due to the reallocation of the Hector Helmholtz layer and the space charge layer reducing the carrier number.[56]

As is well-known, the key to the practical application of photocatalysts is the stability and durability. To evaluate the stability and durability of the CQDs/g-C$_3$N$_4$, a time-circle experiment was performed. Fig. 12 shows the photoelectrocatalytic properties of the 5-CQDs/g-C$_3$N$_4$ over five cycles of organic degradation tests. The CQD/g-C$_3$N$_4$ sample exhibited reproducible photoelectrocatalytic properties after five cycles with only a slight decrease in the efficiency from 97.2% to 85.4%. Minor loss of catalyst may result in the slight decrease of the PEC performance during the recycling experiments. These results indicate an excellent durability and stability of the CQD/g-C$_3$N$_4$ sample. In order to explore the mechanism process of the photocatalyst degradation for organic pollutants, an active species quenching experiment was conducted using nitrogen (N$_2$), isopropyl alcohol (IPA) and ethylenediaminetetraacetate (EDTA-2Na) as the ·O$_2^-$, ·OH and h$^+$ scavengers, respectively. As shown in Fig. 12b, by adding the different quenching agents into the degradation solution, the active species could be
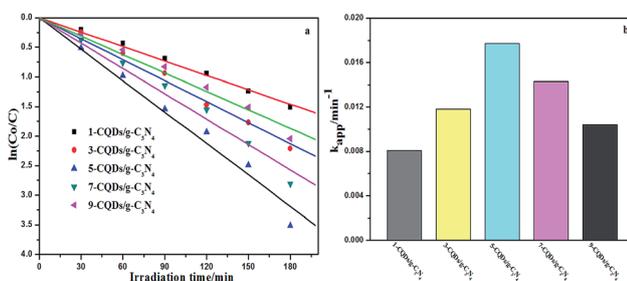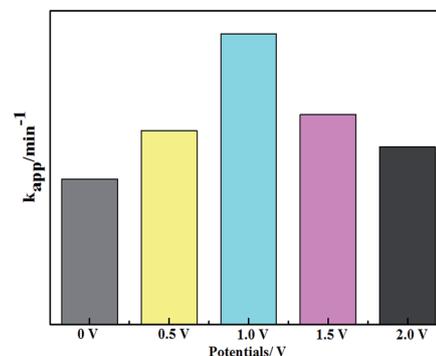

Fig. 10 (a) Photoelectrocatalytic degradation of MB on different electrodes in 0.1 M Na$_2$SO$_4$ under visible light irradiation. (b) The corresponding degradation rate constants.

Fig. 11 Photoelectrocatalytic degradation of MB on the 5-CQD/g-C$_3$N$_4$ electrode at various potentials.
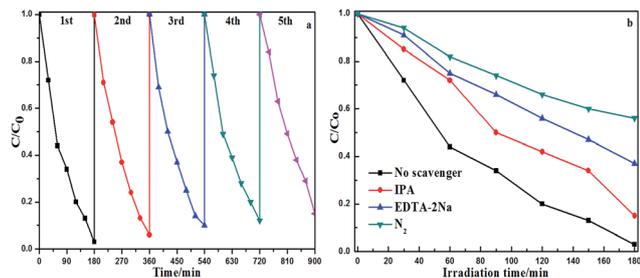
Fig. 12 (a) The recycled 5-CQD/g-C$_3$N$_4$ PEC performance test; and (b) radical trapping experiments during the photocatalytic degradation of MB over the 5-CQD/g-C$_3$N$_4$ composite.

revealed. The photocatalytic performance had different levels of decrease with the addition of the different quenching agents. The degradation efficiency of MB was reduced from 97.21% to 85.02%, 62.64% and 43.75%, respectively, indicating that $\cdot O_2^-$, $\cdot OH$ and h^+ are the active species in the degradation process and $\cdot O_2^-$ is the major active species.

The intermediate products in the degradation process could be quantitatively analyzed and confirmed *via* high-performance liquid chromatography (HPLC).[57] HPLC analyses of phenol solutions degraded by the PEC processes are shown in Fig. 13. As is shown in Fig. 13a, the degradation ability of the photocatalysts for phenol is similar to that for methylene blue (Fig. 9a). The photoelectrocatalytic (PEC) process for the 5-CQDs/g-C$_3$N$_4$ showed the highest degradation efficiency, degrading 51.6% of phenol after 3 h. The HPLC chromatograms for the phenol solutions with the 5-CQDs/g-C$_3$N$_4$ are also shown in Fig. 13b. The characteristic peak of phenol may be seen at
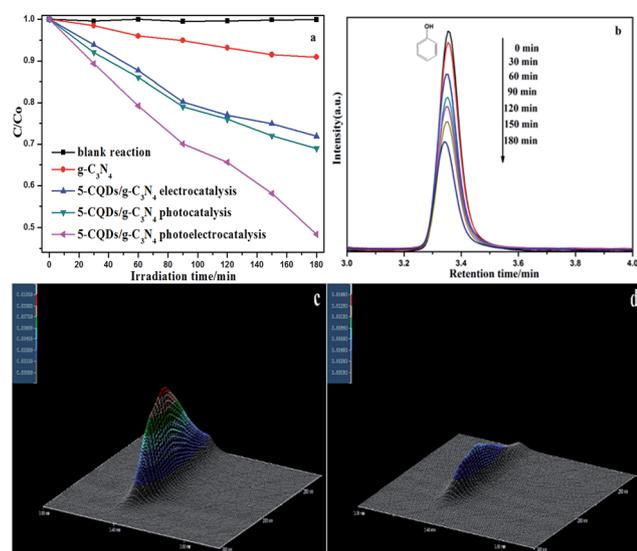
a retention time (RT) of 3.35 min. Based on the retention time and peak positions, the three-dimensional HPLC chromatographs are shown to further demonstrate the photoelectrocatalytic activity of the 5-CQDs/g-C$_3$N$_4$. As shown in Fig. 13c, the peaks corresponding to phenol in the chromatogram for the reaction at 0 min can be seen. After 180 min of illumination, the corresponding phenol peaks decreased in the chromatogram (Fig. 13d). Furthermore, there were no impurity peaks, suggesting that phenol could be mineralized to CO$_2$ or H$_2$O in the photocatalytic reaction process.

To better understand the process, a transient photocurrent response experiment was performed. The prompt photocurrent response of the as-prepared materials corresponded well to the on/off cycles of the visible light irradiation (Fig. 14). A significantly higher photocurrent was observed for the CQD/g-C$_3$N$_4$ electrode in comparison to that for the g-C$_3$N$_4$ electrode. This indicates that the electron transfer from g-C$_3$N$_4$ to the CQDs upon irradiation favors an effective charge separation[58] and was in accordance with the PL analysis. Additionally, the photocurrent of the CQDs/g-C$_3$N$_4$ continuously decreased and then stabilizes after about 600 s and finally dropped by 30%. This may be due to some photocatalyst falling off from the electrode in the reaction process.

The interfacial charge transfer properties of the electrodes could be characterized *via* electrochemical impedance spectroscopy (EIS). Generally, the diameter of the curve in a Nyquist plot is equal to the charge transfer resistance of the electrode surface, and a small diameter is related to a low resistance.[59] Fig. 15a shows the Nyquist plot for the prepared g-C$_3$N$_4$ and 5-CQD/g-C$_3$N$_4$ samples. It was found that the 5-CQDs/g-C$_3$N$_4$ have a lower resistance value than g-C$_3$N$_4$, which is consistent with the above PL analysis results. This means that the introduction of the CQDs leads to an effective separation of the e$^-$–h$^+$ pairs and a faster interfacial charge transfer. Fig. 15b shows that the characteristic frequency peaks for g-C$_3$N$_4$ and the 5-CQDs/g-C$_3$N$_4$ are located at 14.7 Hz and 2.6 Hz, respectively. According to the electron lifetime formula ($\tau \approx 1/(2\pi f)$),[60] the electron lifetime (τ) of the 5-CQDs/g-C$_3$N$_4$ was estimated to be 61.2 ms, which is 5.7 times higher than that of g-C$_3$N$_4$ (10.8 ms). This indicates an efficient inhibited charge recombination and a higher injected electron lifetime in the CQD/g-C$_3$N$_4$ photoelectrode.
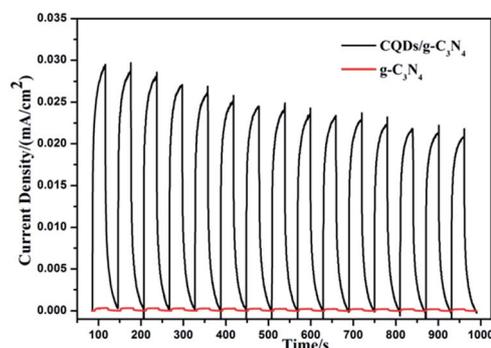

Fig. 13 (a) Different phenol degradation processes over the g-C$_3$N$_4$ and 5-CQD/g-C$_3$N$_4$ photoelectrodes. (C_{phenol}: 5 ppm; $C_{Na_2SO_4}$: 150 mg L^{-1}) (b) HPLC chromatograms of the phenol solutions over the 5-CQDs/g-C$_3$N$_4$. (c) Three-dimensional HPLC chromatographic spectra of the phenol PEC degradation (0 min). (d) Three-dimensional HPLC chromatographic spectra of the phenol PEC degradation (180 min).

Fig. 14 The transient photocurrent response for g-C$_3$N$_4$ and the CQDs/g-C$_3$N$_4$.
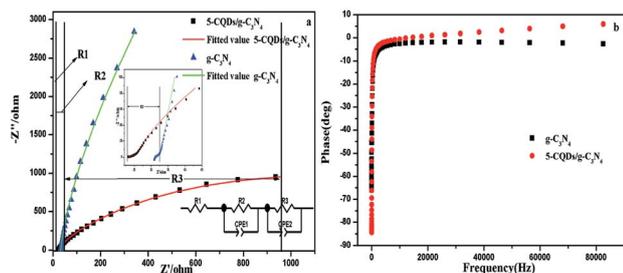
Fig. 15 (a) Electrochemical impedance spectra and (b) the Bode-phase for g-C_3N_4 and the 5-CQDs/g-C_3N_4.

In the PEC degradation process for organic pollutants, a synergistic effect could be produced to combine electro-catalysis (EC) with photocatalysis (PC). The irradiation of visible light may not only generate a promotional effect for EC oxidation but also eliminate the electrode passivation. As is shown in Fig. 16, a number of $e^- - h^+$ pairs may be generated in g-C_3N_4 under visible light irradiation. When the CQD/g-C_3N_4 film electrode experiences a sufficient bias potential, some photo-generated electrons may be quickly and efficiently moved to the platinum electrode (Pt) through the external circuit. This charge transport process could promote the rate of separation of the $e^- - h^+$ pairs and enhance the PEC performance. Furthermore, as the responsible electron reservoirs, the CQDs may trap emitted e^- from the CB of g-C_3N_4. Thus, the e^- in the g-C_3N_4 conduction band could be removed to the CQDs, and then react with molecular oxygen to produce superoxide anion radicals ($\cdot O_2^-$), which participate in the oxidation of organic pollutants. Meanwhile, the h^+ in the VB will transmit to the surface of g-C_3N_4, and react with hydroxyl species to form active hydroxyl radicals ($\cdot OH$), or react with surface-adsorbed organic pollut-ants directly. Considering the above, the efficiency of the degradation of organic pollutants could be improved through the significant synergies of the photocatalytic and electro-catalytic oxidation processes.
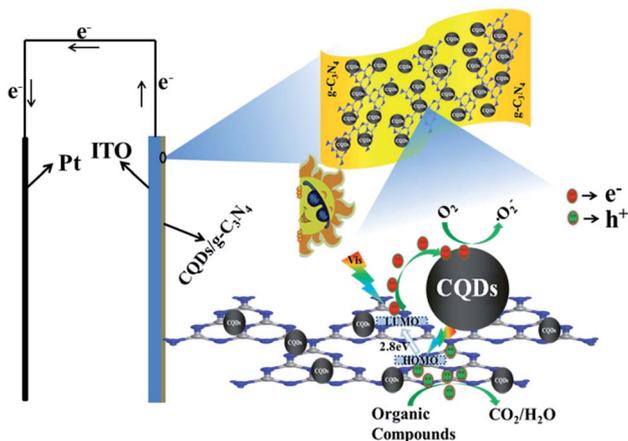
4. Conclusions

In conclusion, we report that CQDs/g-C_3N_4 show a high pho-toelectrocatalytic activity and long-term stability for the degra-dation of organic pollutants (methylene blue and phenol) under visible light irradiation. The 5-CQD/g-C_3N_4 composite effec-tively degraded methylene blue (97.2%) and phenol (51.6%) at a 1.0 V bias voltage over 3 h. The enhanced photoelectrocatalytic activity of the CQD/g-C_3N_4 composites may be attributed to the surface hybrid hetero-junction structures between the g-C_3N_4 nanosheets and the CQDs. This hetero-junction may evidently promote the rate of separation of the photogenerated $e^- - h^+$ pairs, and thus improve the efficiency of the PEC process. Additionally, the synergistic effects between electrocatalysis and photocatalysis obviously improve the efficiency of the organic pollutant degradation, making an effective method to deal with organic wastewater. These findings provide a deep insight into the interaction modes of CQDs with photocatalysts, and also provide a new approach to improve the stabilities of photo-catalysts. This typical metal-free composite photocatalyst is low-cost and environmentally friendly, and shows excellent thermal and chemical stabilities, and is accompanied with a highly conjugated band structure, and is promising for semiconductor composites and new energy applications.

Conflicts of interest

The authors declare that they have no conflicts of interest.

Acknowledgements

Notes and references

1 Y. F. Sun, S. Gao and Y. Xie, *Chem. Soc. Rev.*, 2014, **43**, 530–546.

2 R. T. Lv, J. A. Robinson, R. E. Schaak, D. Sun, Y. F. Sun, T. E. Mallouk and M. Terrones, *Acc. Chem. Res.*, 2015, **48**, 56–64.

3 Y. F. Zhao, G. B. Chen, T. Bian, C. Zhou, G. I. N. Waterhouse, L. Z. Wu, C. H. Tung, L. J. Smith, D. O'Hare and T. R. Zhang, *Adv. Mater.*, 2015, **27**, 7824–7831.

4 Y. Peng, L. Shang, T. Bian, Y. F. Zhao, C. Zhou, H. J. Yu, L. Z. Wu, C. H. Tung and T. R. Zhang, *Chem. Commun.*, 2015, **51**, 4677–4680.

5 Y. F. Sun, S. Gao, F. C. Lei, C. Xiao and Y. Xie, *Acc. Chem. Res.*, 2015, **48**, 3–12.

6 A. Thomas, A. Fischer, F. Goettmann, M. Antonietti, J. O. Muller, R. Schlogl and J. M. Carlsson, *J. Mater. Chem*, 2008, **18**, 4893–4908.

Fig. 16 Mechanism of the photoelectrocatalytic process for the CQDs/g-C_3N_4 under visible light irradiation.

7 X. C. Wang, K. Maeda, A. Thomas, K. Takanabe, G. Xin, J. M. Carlsson, K. A. Domen and M. Antonietti, *Nat. Mater.*, 2009, **8**, 76–80.

8 X. C. Wang, S. Blechert and M. Antonietti, *ACS Catal.*, 2012, **2**, 1596–1606.

9 Y. Wang, X. C. Wang and M. Antonietti, *Angew. Chem., Int. Ed.*, 2012, **51**, 68–89.

10 J. S. Zhang, F. S. Guo and X. C. Wang, *Adv. Funct. Mater.*, 2013, **23**, 3008–3014.

11 Y. W. Zhang, J. H. Liu, G. Wu and W. Chen, *Nanoscale*, 2012, **4**, 5300–5303.

12 A. J. Du, S. Sanvito, Z. Li, D. W. Wang, Y. Jiao, T. Liao, Q. Sun, Y. H. Ng, Z. H. Zhu, R. Amal and S. C. Smith, *J. Am. Chem. Soc.*, 2012, **134**, 4393–4397.

13 Q. J. Xiang, J. G. Yu and M. Jaroniec, *J. Phys. Chem. C*, 2011, **115**, 7355–7363.

14 Y. B. Li, H. M. Zhang, P. R. Liu, D. Wang, Y. Li and H. J. Zhao, *Small*, 2013, **9**, 3336–3344.

15 G. Z. Liao, S. Chen, X. Quan, H. T. Yu and H. M. Zhao, *J. Mater. Chem.*, 2012, **22**, 2721–2726.

16 K. Dai, L. H. Lu, Q. Liu, G. P. Zhu, X. Q. Wei, J. Bai, L. L. Xuan and H. Wang, *Dalton Trans.*, 2014, **43**, 6295–6299.

17 R. C. Pawar, S. Kang, S. H. Ahn and C. S. Lee, *RSC Adv.*, 2015, **5**, 24281–24292.

18 Y. L. Chen, J. H. Li, Z. H. Hong, B. Shen, B. Z. Lin and B. F. Gao, *Phys. Chem. Chem. Phys.*, 2014, **16**, 8106–8113.

19 L. X. Chen, H. Tao, T. Pang, J. F. Dong and X. F. Song, *Chem.Lett.*, 2015, **44**, 348–350.

20 S. Y. Lim, W. Shen and Z. Q. Gao, *Chem. Soc. Rev.*, 2015, **44**, 362–381.

21 J. Liu, Y. Liu, N. Y. Liu, Y. Z. Han, X. Zhang, H. Huang, Y. Lifshitz, S. T. Lee, J. Zhong and Z. H. Kang, *Science*, 2015, **347**, 970–974.

22 J. Di, J. X. Xia, M. X. Ji, L. Xu, S. Yin, Q. Zhang, Z. G. Chen and H. M. Li, *Carbon*, 2016, **98**, 613–623.

23 Y. Q. Dong, N. N. Zhou, X. M. Lin, J. P. Lin, Y. W. Chi and G. N. Chen, *Chem. Mater.*, 2010, **22**, 5895–5899.

24 H. T. Li, X. D. He, Y. Liu, H. Huang, S. Y. Lian, S. T. Lee and Z. H. Kang, *Carbon*, 2011, **49**(2), 605–609.

25 Y. H. Zhang, Z. R. Tang, X. Fu and Y. J. Xu, *ACS Nano*, 2011, **5**, 7426–7435.

26 L. M. Zhang, S. O. Diao, Y. F. Nie, K. Yan, N. Liu, B. Y. Dai, Q. Xie, A. Reina, J. Kong and Z. F. Liu, *J. Am. Chem. Soc.*, 2011, **133**, 2706–2713.

27 J. Xia, J. Di, H. Li, H. Xu, H. Li and S. Guo, *Appl. Catal., B*, 2016, **181**, 260–269.

28 F. Deng, X. Lu, F. Zhong, X. Pei, X. Luo, S. Luo, D. D. Dionysiou and C. Au, *Nanotechnology*, 2016, **27**, 065701.

29 J. Di, J. Xia, Y. Ge, H. Li, H. Ji, H. Xu, Q. Zhang, H. Li and M. Li, *Appl. Catal., B*, 2015, **168–169**, 51–61.

30 F. Nan, Z. Kang, J. Wang, M. Shen and L. Fang, *Appl. Phys. Lett.*, 2015, **106**, 153901–153905.

31 S. Fang, Y. Xia, K. Lv, Q. Li, J. Sun and M. Li, *Appl. Catal., B*, 2016, **185**, 225–232.

32 H. Zhang, H. Huang, H. Ming, H. Li, L. Zhang, Y. Liu and Z. Kang, *J. Mater. Chem.*, 2012, **22**, 10501–10506.

33 D. Yan, Y. Liu, C. Y. Liu, Z. Y. Zhang and S. D. Nie, *RSC Adv.*, 2016, **6**, 14306–14313.

34 G. Li, X. Liu, H. Zhang, T. An, S. Zhang, A. R. Carroll and H. Zhao, *J. Catal.*, 2011, **277**, 88–94.

35 X. Nie, G. Li, M. Gao, H. Sun, X. Liu, H. Zhao, P.-K. Wong and T. An, *Appl. Catal., B*, 2014, **147**, 562–570.

36 X. J. Bai, R. L. Zong, C. X. Li, D. Liu, Y. F. Liu and Y. F. Zhu, *Appl. Catal., B*, 2014, **147**, 82–91.

37 H. Ming, Z. Ma, Y. Liu, K. M. Pan, H. Yu, F. Wang and Z. H. Kang, *Dalton Trans.*, 2012, **41**, 9526–9531.

38 X. Zhao and Y. F. Zhu, *Environ. Sci. Technol.*, 2006, **40**, 3367–3372.

39 M. Groenewolt and M. Antonietti, *Adv. Mater.*, 2005, **17**, 1789–1792.

40 L. Tang, R. Ji, X. K. Cao, J. Y. Lin, H. X. Jiang and X. M. Li, *ACS Nano*, 2012, **6**, 5102–5110.

41 X. H. Gao, H. B. Wu, L. X. Zheng, Y. J. Zhong, Y. Hu and X. W. Lou, *Angew. Chem., Int. Ed.*, 2014, **53**, 5917–5921.

42 H. Wang, Y. H. Liang, L. Liu, J. H. Hu and W. Q. Cui, *Appl. Surf. Sci.*, 2017, **392**, 51–60.

43 K. Li, F. Y. Su and W. D. Zhang, *Appl. Surf. Sci.*, 2016, **375**, 110–117.

44 X. Y. Xia, N. Deng, G. W. Cui, J. F. Xie, X. F. Shi, Y. Q. Zhao, Q. Wang, W. Wang and B. Tang, *Chem. Commun.*, 2015, **51**, 10899–10902.

45 G. K. Zhang, X. M. Ding, F. S. He, X. Y. Yu, J. Zhou, Y. J. Hu and J. W. Xie, *Langmuir*, 2008, **24**, 1026–1030.

46 H. Li, X. He, Z. Kang, H. Huang, Y. Liu, J. Liu, S. Lian, C. H. A. Tsang, X. Yang and S. T. Lee, *Angew. Chem.*, 2010, **122**, 4532–4536.

47 L. Cao, X. Wang, M. J. Meziani, F. Lu, H. Wang, P. G. Luo, Y. Lin, B. A. Harruff, L. M. Veca, D. Murray, S. Y. Xie and Y. P. Sun, *J. Am. Chem. Soc.*, 2007, **129**, 11318–11319.

48 H. J. Yu, Y. F. Zhao, C. Zhou, L. Shang, Y. Peng, Y. H. Cao, L. Z. Wu, C. H. Tung and T. R. Zhang, *J. Mater. Chem.*, 2014, **2**, 3344–3351.

49 J. C. Liu, H. Jeong, J. Z. Liu, K. Lee, J. Y. Park, Y. H. Ahn and S. Lee, *Carbon*, 2010, **48**, 2282–2289.

50 P. Niu, L. L. Zhang, G. Liu and H. M. Cheng, *Adv. Funct. Mater.*, 2012, **22**, 4763–4770.

51 V. N. Khabashesku, J. L. Zimmerman and J. L. Margrave, *Chem. Mater.*, 2000, **12**, 3264–3270.

52 T. Komatsu and T. Nakamura, *J. Mater. Chem.*, 2001, **11**, 474–478.

53 S. Yang, Y. Gong, J. Zhang, L. Zhan, L. Ma, Z. Fang, R. Vajtai, X. Wang and P. M. Ajayan, *Adv. Mater.*, 2013, **25**, 2452–2456.

54 R. J. Candal, W. A. Zeltner and M. A. Anderson, *Environ. Sci. Technol.*, 2000, **34**, 3443–3451.

55 F. F. Liang and Y. F. Zhu, *Appl. Catal., B*, 2016, **180**, 324–329.

56 X. Chen, Y. S. Jun, K. Takanabe, K. Maeda, K. Domen, X. Fu, M. Antonietti and X. Wang, *Chem. Mater*, 2009, **21**, 4093–4095.

57 Y. F. Liu, Y. Y. Zhu, J. Xu, X. Y. Bai, R. L. Zong and Y. F. Zhu, *Appl. Catal., B*, 2013, **142–143**, 561–567.

58 J. Di, J. X. Xia, S. Yin, H. Xu, M. Q. He, H. M. Li, L. Xu and Y. P. Jiang, *RSC Adv.*, 2013, **3**, 19624–19631.

59 A. Leelavathi, G. Madras and N. Ravishankar, *J. Am. Chem. Soc.*, 2014, **136**, 14445–14455.

60 S. M. Sun, W. Z. Wang and L. Zhang, *J. Phys. Chem. C*, 2013, **117**, 9113–9120.